Macroporosity free aluminum alloy weldments through numerical simulation of keyhole mode laser welding

H. Zhao and T. DebRoy[a)]
Department of Materials Science and Engineering, The Pennsylvania State University, University Park, Pennsylvania 16802

(Received 19 December 2002; accepted 19 March 2003)

A transport phenomena-based numerical model is developed to predict the keyhole geometry and temperature profiles in the weldment during laser welding. The model can be used to prevent macroporosity formation during laser welding of aluminum alloys. The experimental results show that the weld metal contains large pores when the welding mode changes from conduction to keyhole mode or vice versa due to changes in welding variables. Based on this observation, the mathematical model predicts macroporosity formation when welding is conducted under conditions where small changes in welding parameters lead to a change in the welding mode. The model has been used to predict the geometry of the keyhole and the fusion zone, and the weldment temperature field for laser beam welding of aluminum alloys 5182 and 5754. The calculated weld pool depth, width, and shape for different welding speeds agreed well with the experimental results. The calculations showed that the keyhole profiles for high-speed welding were asymmetric. Negative beam defocusing resulted in a deeper keyhole than that obtained with positive beam defocusing. The transition from keyhole to conduction mode was more abrupt for negative beam defocusing. The model could predict the formation of macroporosity during laser welding of aluminum alloys 5182 and 5754. The results provide hope that transport phenomena-based models can be useful to prevent the formation of macroporosity during keyhole mode laser welding of aluminum alloys. © *2003 American Institute of Physics.* [DOI: 10.1063/1.1573732]

I. INTRODUCTION

The most effective use of strong light-weight aluminum alloys in automobiles and other manufactured products will require the production of structurally sound, defect-free, and reproducible welds[1–3] in a highly automated, high-volume manufacturing environment. Laser welding is the preferred fabrication method for these alloys. However, an important problem in the laser welding of these alloys is their susceptibility to weld metal porosity, which is a major defect in the laser welding of aluminum alloys. There are two main sources of porosity in the weld metal.[3–6] First, the solubility of hydrogen and other common gases in liquid alloys is much higher than that in the solid alloys. Consequently, porosity can form when dissolved gases are released during solidification and trapped by the solidifying alloys. Pores that result from the rejection of solute gases are characterized by their spherical shape and small size, often less than one micrometer in diameter and are called micropores. Although microporosity in welds is undesirable, they do not typically result in the rejection of the laser welded aluminum alloy parts. A second common source of porosity during laser welding is the type that forms due to imperfect collapse of the keyhole during high-energy laser beam welding. This type of porosity is characterized by their large size, typically larger than ten micrometers in diameter and will be referred to herein as macropores. The formation of macroporosity during fusion welding of aluminum alloys adversely affects mechanical properties of weldments[7] and is a serious problem in the laser welding of these alloys.

A recent study[6] showed that macroporosity was rarely observed in either conduction mode or keyhole mode laser welding of aluminum alloys. However, when the beam power density was just above the threshold value for keyhole formation, an unstable keyhole was formed that collapsed with any small disturbance. As a result, in various cross sections of the same welded sample, the weld pool shapes characteristic of either a conduction or keyhole mode was observed. Macroporosity was formed primarily in this mixed mode of welding due to the instability of the keyhole.

Improved quantitative understanding of keyhole mode laser welding is needed for a better understanding of macroporosity formation and, more importantly, in obtaining a solution of this problem based on scientific principles. Recent applications of transport phenomena in fusion welding have greatly expanded our quantitative understanding of the important physical processes in fusion welding. Examples of such advancements include a better understanding of the evolution of weld metal geometry in both spot[8–10] and linear welds[11,12] and weld metal composition changes owing to both the evaporation of alloying elements[13] and dissolution of gases.[14,15] In addition, transport phenomena have played an important role in recent efforts to quantitatively understand the phase composition,[16,17] grain structure,[18,19] and the inclusion structure[20] in weldments. However, structurally sound welds often contain defects that make them unsuitable for service. The previous modeling efforts for keyhole mode

[a)]Electronic mail: debroy@psu.edu

of welding ignored macroporosity formation during laser welding.

In this study, computational and experimental results are presented to demonstrate that applications of transport phenomena can lead to a better understanding of the formation and prevention of macroporosity during laser welding of aluminum alloys 5182 and 5754. A computer model is developed to calculate the keyhole geometry and weld pool shape and size by considering heat conduction in the weldment and heat of evaporation on the keyhole wall. The model is then applied to better understand and prevent the formation of macroporosity during laser welding of aluminum alloys 5182 and 5754. The modeling approach is based on the fact that during laser welding of aluminum alloys, macroporosity forms when small changes in the welding variables lead to changes in the welding mode, i.e., conduction to keyhole mode and vice-versa. The model predictions of weld pool geometry were compared with the experimental data to validate the model. The effects of both positive and negative defocusing on the nature of transition between the keyhole and conduction modes were examined. It is shown that the model can be used to prevent the formation of macroporosity during laser welding of aluminum alloys 5182 and 5754.

II. BACKGROUND

Previous studies[21–34] have led to significant advances in the understanding of the various physical processes in keyhole mode welding. Swift-Hook and Gick[21] formulated a model of keyhole mode of laser welding by treating the laser beam as a moving line source. They obtained a relationship between the seam width, absorbed laser power, and welding speed based on the heat conduction theory. Andrews and Atthey[22] obtained the keyhole profile based on the energy balance on the keyhole wall, assuming that all of the absorbed laser energy was used for the vaporization of metal. Klemens[23] assumed a circular keyhole with vertical walls that was kept open by a balance between the vapor pressure within the keyhole, surface tension, and hydrodynamic pressure in the melt surrounding the keyhole. The model was able to calculate the shape of the vapor cavity and the molten zone. Mazumder and Steen[24] developed a heat transfer model for a moving Gaussian heat source using the finite difference technique. The model assumed complete absorption of energy at all locations on the surface where the temperature exceeded the boiling point. The model predictions of weld pool geometry were found to be comparable with the experimental results. Dowden *et al.*[25–27] treated the viscous flow in the weld pool during keyhole mode welding. They assumed a slim cylindrical keyhole of known radius in a molten pool that was almost cylindrical but not concentric to the keyhole due to the movement of the beam. The temperature on the keyhole wall was assumed to be the boiling point. The size of the molten pool was determined from the computed temperature profiles.

Kross *et al.*[29] developed a keyhole model in which nonequilibrium evaporation from the keyhole surface, surface tension, hydrostatic and hydrodynamic pressures in the melt, as well as heat conduction into the work piece, were considered. The model could predict the shape, position, and size of the keyhole based on the process parameters and the material properties used. Sudnik *et al.*[30] improved this model so that the energy absorption efficiency is no longer a specified parameter but calculated from the fundamental principles of radiation absorption and energy loss. Metzbower[31] calculated the temperature distribution across the surface of the liquid and the keyhole considering laser power loss due to evaporation. A minimum laser power density required to form a keyhole was calculated.

In situ x-ray transmission imaging studies established[32,33] that the keyhole was not symmetrical with respect to the beam axis for high-speed welding. It was observed that the front keyhole wall had a larger angle of inclination than the rear wall.[32] Arata *et al.*[33] suggested that the bent keyhole shape was caused by inertia and ''wall focusing'' effect that resulted in the difference in energy absorption in different parts of the keyhole wall. Kaplan[34] considered asymmetry of the keyhole by considering the different rates of heat transfer at different regions of the keyhole. The predicted keyhole shape was consistent with that observed experimentally. In his model, the calculated weld pool depth was taken as equal to the depth of the keyhole. This is true only for full penetration welding. For partial penetration welding, the thermal conduction at the bottom of the keyhole will result in a molten pool which is deeper than the keyhole.

A critical review of the previous work indicates the following. (a) Much of the previous research was focused on the calculation of the keyhole geometry and temperature profiles in the weldment. (b) Previous research indicated that the temperature on the keyhole surface can be assumed to be the boiling point of the alloy.[21–27,34] This assumption was shown to result in the correct prediction of weld pool geometry. (c) Since the temperature on the keyhole wall is known, it is not necessary to solve equations of conservation of mass, momentum, and energy in vapor, liquid, and solid regions to get temperature field in the weldment and keyhole geometry. (d) The available models have not been used to predict macroporosity formation during laser welding of aluminum alloys.

III. EXPERIMENT

Bead on plate autogenous welds were produced using a 3.0 kW continuous-wave Nd:YAG laser on 1.0 mm and 1.45 mm thick plates of 5182 and 5754 aluminum alloys, respectively. Both alloys were in the annealed condition prior to welding. The beam was delivered using a 600 μm diameter fiber of fused silica to a $f2$ focus optics manipulated through a micropositioning stage mounted on a linear translation device. The beam radius at the focal point was 300 μm. An ancillary copper nozzle having a 8.0 mm inside diameter was utilized to provide shielding gas. This gas nozzle was directed opposite to the direction of travel at an angle of 30° with the workpiece. During welding, the aluminum plates were placed horizontally on a copper backplate. The backplate had a U-shaped groove of 2.0 mm width and 1.5 mm depth under the weld region. Therefore, the liquid metal was not supported by the backplate. Helium was used as the

shielding gas. The effect of laser beam defocusing was evaluated by altering the distance between the workpiece and the optics to obtain defocusing distances in the range from −2.0 mm to +2.0 mm.

IV. MATHEMATICAL MODEL

A. Assumptions and salient features

The following assumptions are made in the model: (1) The temperature on the keyhole wall is assumed to be equal to the boiling point of the alloy. At this temperature, the equilibrium pressures of all the alloying elements add up to 1 atm. Since the keyhole is exposed to the atmosphere, this assumption is justified. (2) Heat transfer rates in directions perpendicular to the laser beam axis along horizontal planes are much larger than those parallel to the beam axis. Since the keyhole is oriented almost vertically, and the surface temperature on the keyhole wall is the boiling point of the alloy, heat is transported mainly along the horizontal plane. (3) Plasma in the keyhole is assumed to have a constant absorption coefficient independent of location. Although this assumption cannot be rigorously defended, it greatly simplifies calculations. Furthermore, the energy loss owing to absorption of laser energy by the plasma is known to be small during Nd:YAG laser welding. Therefore, the error in the computed laser beam intensity and temperature field resulting from this simplification is small. (4) The surface of the keyhole is assumed to be free of oxides and the Fresnel absorption coefficient is assumed to be constant at all locations on the surface.

Four groups of input data are necessary to run the model: material properties, welding parameters, geometrical parameters, and computational parameters. The output of the model includes the geometry of the keyhole when the keyhole forms and a three-dimensional temperature field of the weldment. If a stable keyhole can be formed, the keyhole geometry is calculated based on point-by-point energy balance on the keyhole wall. The model then calculates the three-dimensional temperature field in the weldment. If a stable keyhole cannot be formed for the given welding conditions, the calculations are done considering conduction mode. The heat of evaporation is taken into account in the calculations. The energy absorption by the plasma and the enhanced energy absorption by multiple reflections within the keyhole are also considered.

B. Energy balance on the keyhole wall

As illustrated in Fig. 1, the local keyhole wall angle θ is determined by the balance between the heat flux conducted into the keyhole wall, I_c, the locally absorbed beam energy flux, I_a, and the evaporative heat flux, I_v. The heat balance on the keyhole wall requires $(I_a - I_v)\sin\theta = I_c \cos\theta$. Therefore, we have

$$\tan(\theta) = \frac{I_c}{I_a - I_v}. \tag{1}$$

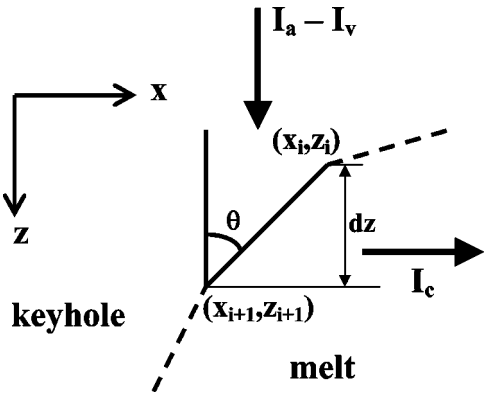

FIG. 1. The relationship between the net absorbed energy flux, $I_a - I_v$, and the heat flux conducted into the metal, I_c, determines the keyhole wall angle θ.

The calculation of local keyhole angle θ requires values of I_c, I_a, and I_v. The procedure for the calculation of these variables is discussed next.

1. Calculation of I_c

The two-dimensional temperature field in an infinite plate can be calculated considering the conduction heat from the keyhole wall into the plate as:[35]

$$T(r,\varphi) = T_a + \frac{P'}{2\pi\lambda_{\text{th}}} K_0(Pe'r) e^{-Pe'r\cos\varphi}, \tag{2}$$

where (r,θ) designates a location in the plate with the line source as the origin, T_a is the ambient temperature, P' is the strength of the line source, i.e., power per unit depth, λ_{th} is the thermal conductivity, $K_0(\,)$ is the second kind and zeroth-order solution of the modified Bessel function, and $Pe' = v/(2\kappa)$, where v is the welding speed and κ is the thermal diffusivity. The radial heat flux in any direction r in the horizontal plane is obtained by differentiating both sides of Eq. (2) with respect to r as

$$I_c(r,\varphi) \approx -\lambda_{\text{th}} \frac{\partial T(r,\varphi)}{\partial r} = \frac{P'}{2\pi} Pe' [K_0(Pe'r)\cos\varphi + K_1(Pe'r)] e^{-Pe'r\cos\varphi}, \tag{3}$$

where $K_1(\,)$ is the second kind and first-order solution of the modified Bessel function. The strength of the line source P' in Eq. (2) can be determined by assuming that the temperature at the keyhole wall reaches the boiling point, T_b:

$$P' = (T_b - T_a) 2\pi\lambda_{\text{th}} \frac{1}{K_0(Pe'r)} e^{Pe'r\cos\varphi}. \tag{4}$$

The heat flux at any point on the keyhole wall can be obtained by combining Eqs. (3) and (4):

$$I_c(r,\varphi) = (T_b - T_a)\lambda_{\text{th}} Pe' \left(\cos\varphi + \frac{K_1(Pe'r)}{K_0(Pe'r)} \right), \tag{5}$$

where $\varphi = 0$ at the front keyhole wall and $\varphi = \pi$ at the rear keyhole wall. Therefore, at the front keyhole wall,

$$I_c(x_{fs},0)=(T_b-T_a)\lambda_{th}Pe'\left(1+\frac{K_1(Pe'x_{fs})}{K_0(Pe'x_{fs})}\right), \quad (6)$$

where x_{fs} is the distance between the line source and the front keyhole wall. A similar expression can be written for the rear keyhole wall.

2. Calculation of I_a

The locally absorbed beam energy flux, I_a, on the keyhole wall is calculated by taking into account the Fresnel absorption by the workpiece during multiple reflections and the plasma absorption. As indicated in the Appendix, the absorbed beam energy flux is given by

$$I_a=e^{-\beta 1}[1-(1-\alpha)^{\pi/(4\bar{\theta})}]I_0, \quad (7)$$

where β is the inverse Bremsstrahlung absorption coefficient of plasma, 1 is the average path of the laser beam in plasma before it reaches the keyhole wall, α is the Fresnel absorption coefficient of the work piece, $\bar{\theta}$ is the average angle between the keyhole wall and the initial incident beam axis, and I_0 is the local incident beam intensity and is given by[36]

$$I_0=I_{f0}\left(\frac{r_{f0}}{r_f}\right)^2\exp\left(-\frac{r^2}{r_f^2}\right), \quad (8)$$

where I_{f0} is the peak intensity at the focal point, given by $2P/(\pi r_{f0}^2)$, P is the laser power, r_{f0} is the beam radius at the focal point, r_f is the local beam radius, given[36] by

$$r_f=r_{f0}\left[1+\left(\frac{z+z_0}{2r_{f0}f/d_b}\right)^2\right]^{1/2}, \quad (9)$$

where z_0, f, and d_b are the beam defocusing, beam focal length, and beam diameter on the optics, respectively. The value of z_0 is positive when the focal point is above the work piece surface and is negative when the focal point is below the work piece surface.

3. Calculation of I_v

The evaporative heat flux, I_v, on the keyhole wall is calculated from

$$I_v=\sum_{i=1}^{n} J_{v,i}\Delta H_{v,i}, \quad (10)$$

where n indicates the total number of alloying elements in the alloy, $J_{v,i}$ is the evaporation flux of element i, and $\Delta H_{v,i}$ is the heat of evaporation. The evaporation flux at very low pressures can be accurately calculated from the Langmuir equation.[37–39] However, at one atmosphere pressure, the Langmuir equation significantly overpredicts the vaporization rate. Based on previous studies,[38,39] the calculated evaporation flux using the Langmuir equation is usually five to ten times higher than the experimental results. In this study, a factor of 7.5 is used to calculate the evaporation flux from the modified Langmuir equation:

$$J_{c,i}=\frac{44.34}{7.5}a_i P_i^{\circ}\sqrt{\frac{M_i}{T_b}}, \quad (11)$$

where a_i is the activity of element i in the liquid metal, P_i° is the equilibrium vapor pressure of element i over pure liquid at the boiling point T_b, and M_i is the molecular weight of element i.

C. Keyhole wall profile and temperature field

Assuming that the beam axis is located at $x=0$ and $y=0$, the following relation can be derived from Eq. (2):

$$\frac{e^{Pe'x_{fs}}}{K_0(Pe'x_{fs})}=\frac{e^{-Pe'x_{rs}}}{K_0(Pe'x_{rs})}. \quad (12)$$

Equation (12) can be solved, considering $x_{fs}+x_{rs}=x_f-x_r$, to obtain x_{fs} and x_{rs}. The position of line source is then calculated from $x_s=x_f-x_{fs}$. The heat fluxes on the front and rear keyhole wall, $I_c(x_{fs})$ and $I_c(x_{rs})$, are calculated from Eq. (6) and a relation similar to Eq. (6) using the known values of x_{fs} and x_{rs}. The local angles of the front and rear keyhole walls are calculated from Eq. (1). The keyhole wall positions at the next depth (z) value can be determined from the current positions and the local angles. Using the calculated position of front (or rear) keyhole wall, the strength of the line source at any given depth, z, is calculated from Eq. (4). Using the calculated strength P', and the location, x_s, of the line source, the temperature field in $x-y$ plane at each depth, z, is calculated by:

$$T(x,y)=T_a+\frac{P'}{2\pi\lambda_{th}}K_0(Pe'\sqrt{(x-x_s)^2+y^2})\times e^{-Pe'(x-x_s)/\sqrt{(x-x_s)^2+y^2}}. \quad (13)$$

When the depth of the keyhole is less than the plate thickness, the temperature field below the bottom of the keyhole cannot be calculated from Eq. (13). To calculate the temperature field in this domain, the following heat diffusion equation is solved:

$$\frac{\partial^2 T}{\partial x^2}+\frac{\partial^2 T}{\partial y^2}+\frac{\partial^2 T}{\partial z^2}-\frac{v}{\kappa}\frac{\partial T}{\partial x}=0. \quad (14)$$

The boundary conditions necessary to solve Eq. (14) are as follows. The top surface of the domain is the $x-y$ plane at the bottom of the keyhole. The temperature on this plane is obtained from Eq. (13). The boundary condition for the bottom surface is given by

$$J(x,y,z)|_{z=\max}=h[T_a-T(x,y,z)|_{z=\max}], \quad (15)$$

where $J(x,y,z)$ is the heat flux, h is the heat transfer coefficient, T_a is the ambient temperature, and $T(x,y,z)$ is the local temperature. The temperatures on other surfaces of the domain are assumed to be ambient temperature since the surfaces are far away from the heat source. The data used in the calculations are presented in Table I.

V. RESULTS AND DISCUSSION

A typical computed keyhole profile is shown in Fig. 2. The beam profile is also shown in Fig. 2. It is observed that the beam axis intersects the front keyhole wall. Furthermore, the front keyhole wall has a larger angle with the beam axis than does the rear keyhole wall. The asymmetry of the key-

TABLE I. Material properties and process parameters.

Material	Aluminum alloy 5182	Aluminum alloy 5754
Ambient temperature, T_a	298 K	298 K
Melting point, T_m	850 K[a]	880 K
Boiling point, T_b	1930 K[b]	2015 K
Density, ρ	2300 kg/m^3[c]	2300 kg/m^3
Thermal conductivity, λ_{th}	108 W/m-K[c]	138 W/m K
Specific heat, C_p	1200 J/kg-K[c]	1250 J/kg K
Thermal diffusivity, κ	3.9×10^{-5} m^2/s	4.8×10^{-5} m^2/s
Heat of fusion, ΔH_f	3.95×10^5 J/kg[c]	3.95×10^5 J/kg
Laser power, P	2.5 kW	3.0 kW
Fresnel absorption, α	0.14[d]	
Inverse Bremsstrahlung absorption coefficient, α_p	100 m^{-1}[e]	
Welding speed, v	0.064–0.13 m/s (150–300 ipm)	
Beam focal length, f	0.078 m	
Beam radius on optics, $d_b/2$	0.028 m	
Beam radius at focal point, r_{f0}	3.0×10^{-4} m	
Beam defocusing, z_0	−0.0025 to 0.0025 m	

[a]See Ref. 40.
[b]See Ref. 13.
[c]See Ref. 41.
[d]See Ref. 42.
[e]See Ref. 34.

hole shape was caused by the different temperature gradients and the resulting heat fluxes near the front and the rear walls. The difference in the heat fluxes in the two walls is consistent with the asymmetric keyhole shape experimentally obtained by an *in situ* x-ray transmission imaging system.[32,33] The calculated three-dimensional temperature field for this welding condition is given in Fig. 3. During welding, the laser beam encounters cold material near the front keyhole wall. The material near the rear wall has already been heated. As a result, the temperature gradient near the front keyhole wall is much higher than that near the rear wall as observed in Fig. 3. Consequently, the heat flux into the front wall is higher than that into the rear wall. Therefore, according to Eq. (1), the front wall should have a larger angle since the heat flux into the front wall, I_c, is larger for the same net absorbed heat flux, $I_a - I_v$.

The experimental and calculated weld pool cross sections for different welding speeds are shown in Fig. 4 for the welding of alloy 5182. The isotherms for 1930 K, 1450 K, 1050 K, and 850 K are shown in each of the calculated weld pool cross sections. The isotherm for solidus temperature 850 K gives the outline of the calculated molten pool. It is observed that the calculated weld pool geometry is consistent with the experimental results. At a welding speed of 64 mm/s, the keyhole depth was equal to the plate thickness and a full penetration welding was obtained. All of the isotherms were roughly parallel to the beam axis, indicating that the heat conduction was two-dimensional and heat transfer occurred mainly along the horizontal plane. At higher welding speeds, the keyhole depths were less than the plate thickness and partial penetration welds were obtained.

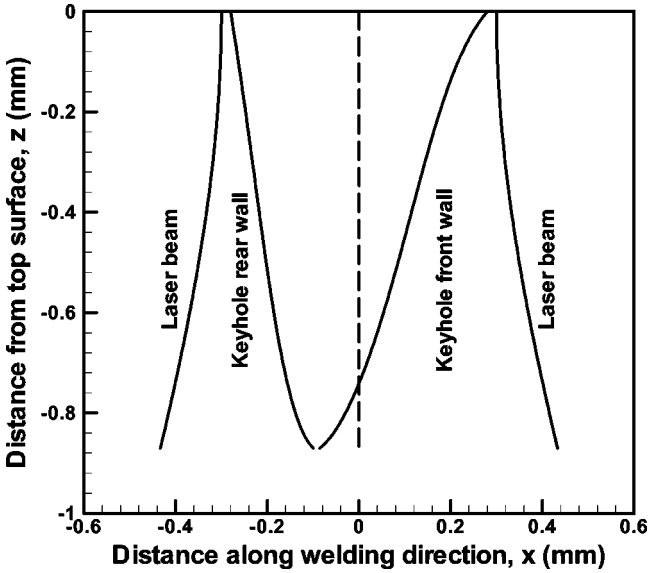

FIG. 2. Keyhole profile along the symmetry plane. Alloy: 5182, power: 2.5 kW, speed: 106 mm/s, and defocus: 0 mm.

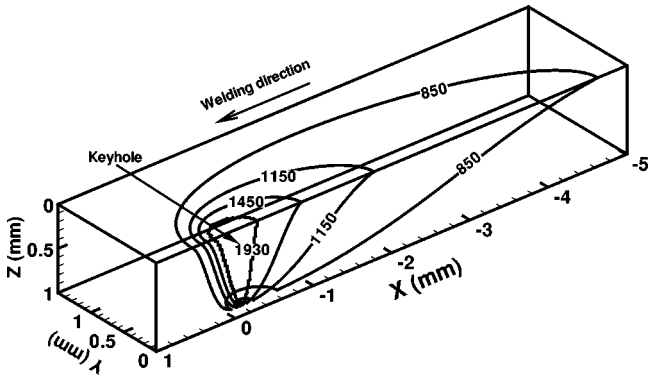

FIG. 3. Computed temperature field. Alloy: 5182, power: 2.5 kW, speed: 106 mm/s, and defocus: 0 mm. The values on the temperature isotherms are in K.

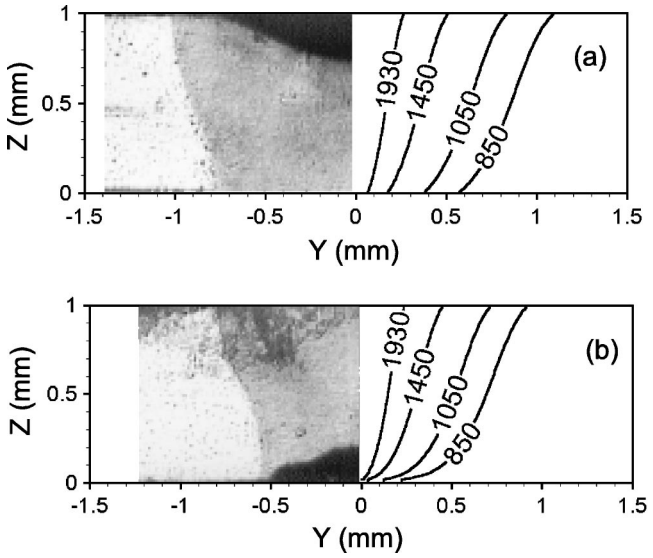

FIG. 4. Comparison of the experimentally determined weld pool cross sections at different welding speeds with the calculated results. The contour values indicate temperatures in K. Alloy: 5182, power: 2.5 kW, and defocus: 0 mm. Welding speeds were 0.063 m/s and 0.085 m/s for the results in (a) and (b), respectively.

The calculated weld pool depths in the laser welded aluminum alloy 5182 for different beam defocusing values are compared with the experimental values in Fig. 5. Three sets of experimental data are included in Fig. 5. A nomenclature of positive defocusing to represent the focal point to be above the top surface of the workpiece and negative defocusing to represent the focal point to be below the top surface will be used throughout this article. It is observed that the calculated weld pool depths agree well with the experimental data. For the welding conditions considered here, three distinct regimes are identified based on the mode of welding depending on the beam defocusing. These three regimes are stable keyhole, unstable keyhole, and conduction mode welding. When the beam is highly defocused, the beam intensity is well below the threshold value to form a keyhole, resulting in conduction mode welding characterized by roughly a hemispherical weld pool shape. When the beam is nearly focused, the beam intensity is well above the threshold value to form a stable keyhole, resulting in deep weld pool characteristic of keyhole mode welding. The keyhole becomes unstable where the beam intensity is almost equal to the threshold value for keyhole formation, i.e., between the regimes of conduction mode and stable keyhole mode. The welding mode in this intermediate region is unpredictable. Any small disturbance in a welding variable such as the laser power can cause the welding mode to shift between the keyhole and the conduction modes. As a result, in various cross sections of the same welded sample, the weld pool shapes characteristic of either the conduction or keyhole mode was observed.

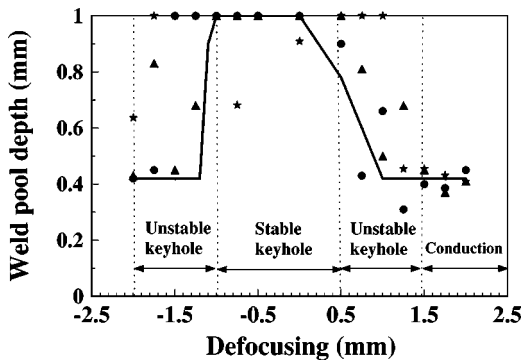

FIG. 5. Comparison of the computed weld pool depth at several welding speeds with the experimental results. Alloy: 5182, power: 2.5 kW, speed: 106 mm/s, and defocus: 0 mm. The three symbols refer to three sets of experiments.

Based on the experimentally determined weld pool depths shown in Fig. 5, keyholes were formed for beam defocusing values in the range of about -1.0 to 0.6 mm. It is observed from Fig. 5 that for positive beam defocusing, the keyhole depth dropped rapidly as the beam defocusing increased from 0.5 to 1.0 mm. This region can be considered as the transition region between stable keyhole to conduction modes. On the other hand, the predicted transition region for negative defocusing is more abrupt, which is a very small region near a beam defocusing value of -1.0 mm. These differences in using positive and negative beam defocusing have been observed in an earlier study of laser welding of stainless steel[31] and can be explained from the interactions between the beam and the keyhole. For highly negative beam defocusing, the beam is convergent and its intensity increases with the deepening of the keyhole, promoting the formation of a deeper keyhole. The increasing beam intensity with the keyhole depth causes the keyhole depth to be very deep when the keyhole forms. When the beam defocusing value is lower than -1.0 mm, the keyhole does not form as shown in Fig. 5. On the other hand, for positive beam defocusing, the beam is divergent and its intensity decreases vertically downward along the keyhole depth, restricting further deepening of the keyhole. The decreasing beam intensity with the keyhole depth causes the keyhole depth to decrease more gradually with an increase in the positive value of beam defocusing.

A previous study[4] showed that the extent of laser beam defocusing greatly affected keyhole formation, weld pool geometry, and macroporosity formation during laser welding of aluminum alloys 5182 and 5754. It was observed that the porosity was minimum when welding was conducted in either the keyhole or conduction mode. In contrast, extensive porosity in the weld metal was observed in the transition region where the keyhole was not stable. Therefore, the formation of macroporosity can be linked to the transition from the keyhole to the conduction mode. In this study, the changes in the mode of welding were predicted for different beam defocusing and compared with the experimental results of porosity and depth of penetration of the weld metal.

The experimental and calculated weld pool depths for laser welded aluminum alloy 5754 plates at several defocusing values are shown in Fig. 6. A good agreement is observed between the experimental and the calculated values. Moreover, the model correctly predicted the transition from stable keyhole to conduction modes and, therefore, the formation of macroporosity during welding. Figure 7 shows the calculated

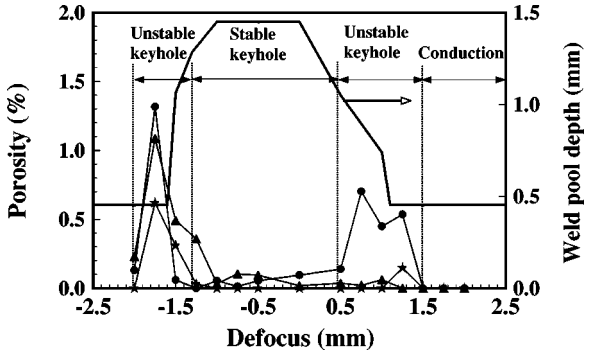

FIG. 6. The experimental (see Ref. 4) and calculated weld pool depths for laser welded 1.45 mm thick aluminum alloy 5754 plates at several defocus values. Laser power: 3.0 kW and speed: 63.5 mm/s. The three symbols refer to three sets of experiments.

keyhole depth and measured porosity in laser welded alloy 5754. Based on the calculated keyhole depth, stable keyhole mode welding was predicted in the range of -1.75 to 1.0 mm for this alloy. As shown in Fig. 7, no significant porosity was observed in the stable keyhole mode or conduction mode. However, at defocus values close to -1.75 mm or 1.0 mm, the welding mode easily switched between the conduction and keyhole modes and a significant amount of porosity was formed. The results show that the model can be used to prevent macroporosity formation through the application of transport phenomena.

VI. SUMMARY AND CONCLUSIONS

A model has been developed for keyhole mode laser beam welding. The keyhole profile was calculated based on point-by-point calculation of the energy balance on the keyhole wall where the temperature was assumed to be equal to the boiling point of the alloy. The three-dimensional temperature field of the weldment was calculated considering heat conduction. The model has been used to predict the mode of welding, the keyhole geometry, and weldment temperature field for the laser welding of aluminum alloys 5182 and 5754. The following are the major conclusions.

(1) The predicted welding mode for different beam defocusing values agreed well with the experimental results. The model can be used to predict the welding mode and, therefore, it can determine the welding conditions where a transition in the mode of welding occurs. The model predicts macroporosity formation when the welding mode changes from the conduction to keyhole modes or vice versa.
(2) The intensity of a convergent (negative defocusing) beam increases, whereas that of a divergent (positive defocusing) beam decreases, with distance inside the keyhole. Due to this difference, welding with negative beam defocusing resulted in a deeper keyhole than with positive beam defocusing. The transition from the keyhole to conduction mode was also more abrupt for negative beam defocusing. The model was able to predict these differences between positive and negative defocusing of the laser beams.
(3) The calculated keyhole profile was asymmetric with the rear wall being steeper than the front wall. This is consistent with the different heat conduction rates at the rear and the front walls. The heat conduction rate at the front wall was faster because of the presence of colder material near the front wall during high-speed laser welding. In order to balance the heat loss, the front wall was more inclined so that more beam energy could be intercepted and absorbed. The asymmetric geometry of the calculated keyhole agreed well with that observed experimentally.
(4) The model could be used to predict the weld pool width, depth, and shape for different welding conditions. The experimentally observed fusion zone geometry was consistent with the theoretically computed solidus temperature profile.

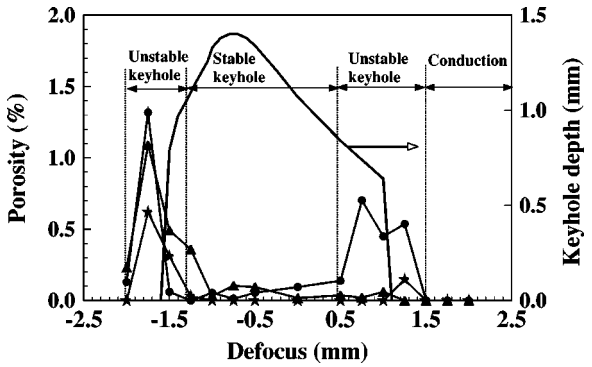

FIG. 7. The calculated keyhole depth and measured porosity (see Ref. 4) at several defocus values in alloy 5754. Laser power: 3.0 kW and welding speed: 63.5 mm/s. The three symbols refer to three sets of experiments.

ACKNOWLEDGMENT

This research was funded by the U.S. Department of Energy (Grant Nos. DE-FG02-96ER45602 and DE-FGO2-01ER45900).

APPENDIX: CALCULATION OF ABSORBED BEAM INTENSITY

Plasma absorption before the beam hits the keyhole wall occurs when a laser beam of intensity I_0 passes through a plasma of length ℓ, part of the beam energy is absorbed by the plasma due to inverse Bremsstrahlung. The beam intensity remaining after absorption can be calculated as[43]

$$I_t = e^{-\beta l} I_0, \tag{A1}$$

where I_t is the intensity transmitted and β is the absorption coefficient.

Absorption by workpiece considering multiple reflections occurs when the beam impinges on the workpiece, part of its energy is absorbed by the workpiece and the remaining part is reflected. The absorbed energy is equal to the product of incident beam energy and the Fresnel absorption coefficient. Assuming a constant Fresnel absorption coefficient, α, independent of the angle of incidence, the fraction of the energy absorbed by the workpiece after n reflections is given by

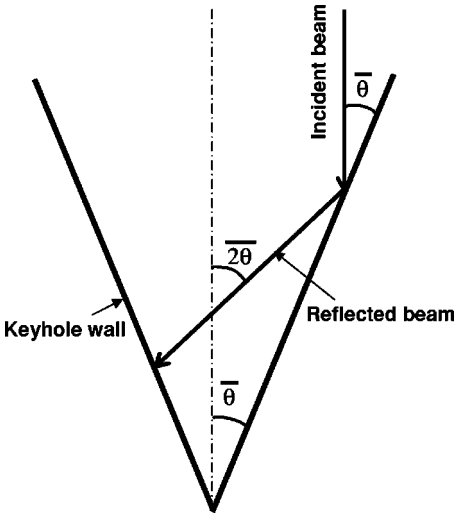

FIG. 8. Schematic diagram showing the angles among the initial incident beam, the reflected beam, and the keyhole wall.

$$\alpha_a = 1-(1-\alpha)^n. \tag{A2}$$

Based on the keyhole profile calculated in the first step of the calculations, the keyhole wall is approximated to be symmetrical for the purpose of the absorption calculations with a mean wall angle of $\overline{\theta}$ as shown in Fig. 8. Based on optical geometry, the angle between the reflected beam and the initial incident beam after n_{mr} reflections is calculated as

$$\theta' = 2n_{mr}\overline{\theta}. \tag{A3}$$

When θ' reaches higher than $\pi/2$, the reflected beam leaves the keyhole without being further absorbed. Therefore, the total number of reflections including the last reflection leaving the keyhole can be calculated from

$$n = n_{mr}+1 = \frac{\pi}{4\overline{\theta}}+1. \tag{A4}$$

The fraction of absorbed beam energy by the workpiece after the multiple reflections is calculated from Eqs. (A2) and (A4) as

$$\alpha_a = 1-(1-\alpha)^{1+\pi/(4\overline{\theta})}. \tag{A5}$$

Total absorption by the work piece occurs by considering both plasma absorption and Fresnel absorption during multiple reflections, the total absorbed beam intensity by the work piece can be obtained by combining Eqs. (A1) and (A5)

$$I_a = \alpha_a I_t = e^{-\beta l}[1-(1-\alpha)^{1+\pi/(4\overline{\theta})}]I_0. \tag{A6}$$

[1] S. A. David and T. DebRoy, Science **257**, 497 (1992).
[2] T. DebRoy and S. A. David, Rev. Mod. Phys. **67**, 85 (1995).
[3] H. Zhao, D. R. White, and T. DebRoy, Int. Mater. Rev. **44**, 238 (1999).
[4] S. Katayama, J. Light Meta. Weld. Construct. **34**, 31 (1996).
[5] D. A. Schauer and W. H. Giedt, Weld. J. (Miami) **57**, 189s (1978).
[6] M. Pastor, H. Zhao, R. P. Martukanitz, and T. DebRoy, Weld. J. (Miami) **78**, 207s (1999).
[7] R. F. Ashton, R. P. Wesley, and C. R. Dixon, Weld. J. (Miami) **54**, 95s (1975).
[8] G. M. Oreper, T. W. Eagar, and J. Szekely, Weld. J. (Miami) **62**, 307s (1983).
[9] C. Chan, J. Mazumder, and M. M. Chen, Metall. Trans. **15A**, 2175 (1984).
[10] W. Pitscheneder, T. DebRoy, K. Mundra, and R. Ebner, Weld. J. (Miami) **75**, 71s (1996).
[11] S. Kou and Y. H. Wang, Metall. Trans. **17A**, 2271 (1986).
[12] K. Mundra, T. DebRoy, and K. Kelkar, Numer. Heat Transfer **29**, 115 (1996).
[13] H. Zhao and T. DebRoy, Metall. Mater. Trans. B **32**, 163 (2001).
[14] K. Mundra, J. M. Blackburn, and T. DebRoy, Sci. Technol. Weld. Joining **2**, 174 (1997).
[15] T. A. Palmer and T. DebRoy, Sci. Technol. Weld. Joining **3**, 190 (1998).
[16] W. Zhang, J. W. Elmer, and T. DebRoy, Mater. Sci. Eng., A **333**, 321 (2002).
[17] Z. Yang, J. W. Elmer, J. Wong, and T. DebRoy, Weld. J. (Miami) **79**, 97s (2000).
[18] Z. Yang, S. Sista, J. W. Elmer, and T. DebRoy, Acta Mater. **48**, 4813 (2000).
[19] S. Sista, Z. Yang, and T. DebRoy, Metall. Mater. Trans. B **31**, 529 (2000).
[20] T. Hong, W. Pitscheneder, and T. DebRoy, Sci. Technol. Weld. Joining **3**, 33 (1998).
[21] D. E. Swift-Hook and A. E. F. Gick, Weld. J. (Miami) **52**, 492s (1973).
[22] J. G. Andrews and D. R. Atthey, J. Phys. D **15**, 2181 (1976).
[23] P. G. Klemens, J. Appl. Phys. **47**, 2165 (1976).
[24] J. Mazumder and W. M. Steen, J. Appl. Phys. **51**, 941 (1980).
[25] J. Dowden, M. Davis, and P. Kapadia, J. Fluid Mech. **126**, 123 (1983).
[26] J. Dowden, N. Postacioglu, M. Davis, and P. Kapadia, J. Phys. D **20**, 36 (1987).
[27] N. Postacioglu, P. Kapadia, M. Davis, and J. Dowden, J. Phys. D **20**, 340 (1987).
[28] P. S. Mohanty and J. Mazumder, Sci. Technol. Weld. Joining **2**, 133 (1997).
[29] J. Kross, U. Gratzke, and G. Simon, J. Phys. D **26**, 474 (1993).
[30] W. Sudnik, D. Radaj, and W. Erofeew, J. Phys. D **29**, 2811 (1996).
[31] E. A. Metzbower, Metall. Trans. B **24**, 875 (1993).
[32] S. Fujinaga, H. Takenaka, T. Narikiyo, S. Katayama, and A. Matsunawa, J. Phys. D **33**, 492 (2000).
[33] Y. Arata, *Plasma, Electron and Laser Beam Technology* (American Society for Metals, Metals Park, OH, 1986).
[34] A. Kaplan, J. Phys. D **27**, 1805 (1994).
[35] D. Rosenthal, Trans. ASME **48**, 848 (1946).
[36] P. Mouroulis and J. Macdonald, *Geometrical Optics and Optical Design* (Oxford University Press, Cambridge, UK, 1997).
[37] A. Block-Bolten and T. W. Eagar, Metall. Trans. B **15**, 461 (1984).
[38] M. M. Collur, A. Paul, and T. DebRoy, Metall. Trans. B **18**, 733 (1987).
[39] P. Sahoo, M. M. Collur, and T. DebRoy, Metall. Trans. B **19**, 967 (1988).
[40] *Properties and Selection—Nonferrous Alloys and Special-purpose Materials*, ASM Handbook vol. 2, 10th ed. (ASM Int. Materials Park, OH, 1990).
[41] J. E. Hatch, *Aluminum: Properties and Physical Metallurgy* (American Society for Metals, Metals Park, OH, 1984).
[42] M. A. Bramson, *Infrared Radiation: A Handbook for Applications* (Plenum, New York, 1968).
[43] D. Williams, *Spectroscopy* (Academic, New York, 1976).